Ultrafine ZnSe/CoSe Nanodots Encapsulated in Core-shell MOFs-Derived Hierarchically Porous N-doped Carbon Nanotubes for Superior Lithium/Sodium Storage

Chuan-Ling Zhang (zhangcl@hfut.edu.cn)
Hefei University of Technology
Qiang Zhang
Hefei University of Technology
Meng-Li Chen
Hefei University of Technology
Xi-Xi Zhu
Hefei University of Technology
Chen-Fan Zhao
Hefei University of Technology
Fu-Hu Cao
Hefei University of Technology
Hao Li
Hefei University of Technology
Huai-Ping Cong
Hefei University of Technology

Research Article

Keywords: ZnSe/CoSe, porous composite nanotubes, lithium/sodium storage, heterointerface, electrospinning

Posted Date: November 21st, 2022

DOI: https://doi.org/10.21203/rs.3.rs-2226251/v1

Abstract

Rational design and development of hierarchical composite structures are of great significance for high-performance lithium-ion and sodium-ion batteries. In this work, core-shell ZIF-8@ZIF-67 nanotubes and polydopamine-derived hierarchically porous N-doped carbon composite with uniformly encapsulated ZnSe/CoSe nanodots (ZnSe@CoSe@CN) were constructed for enhanced lithium/sodium storage. Benefiting from the heterogeneous phase interface of ultrafine ZnSe/CoSe nanodots that can enhance the Li^+/Na^+ diffusion and storage, and the assembled hierarchically porous structured N-doped carbon nanotubes with high electronic conductivity and structural integrity, the bifunctional ZnSe@CoSe@CN anode delivers improved pseudo-capacitive contribution for both lithium and sodium storage, providing excellent rate capabilities (650.8 and 331 mAh g^{-1} at 5 A g^{-1} for lithium and sodium storage, respectively) and long-term cycling stability (a high reversible capacity of 1500 and 622.3 mAh g^{-1} after 100 cycles at 100 mA g^{-1}, and 600 and 397.3 mAh g^{-1} after 1000 cycles at 5 A g^{-1} for lithium and sodium storage, respectively). This work provides an efficient design perspective to construct high-performance electrodes for energy storage devices.

1. Introduction

Rechargeable secondary batteries have attracted great attention due to the severe environmental issues and the emerging new alternative energy demands. Lithium-ion batteries (LIBs) and sodium-ion batteries (SIBs) are promising energy storage candidates on account of their high energy density, high average output voltage, and long cycle life [1–3]. However, the service life and cost are still challenges, especially the sluggish reaction kinetics resulting from the large radius and heavier mass of Na^+ hinder the practical utilization of SIBs [4, 5]. Therefore, designing and preparing LIBs and SIBs electrode materials for enhanced electrochemical performance is of great potential [6, 7]. Up to now, numerous anode materials have been investigated for LIBs and SIBs [8–10]. Among them, metallic selenides (such as ZnSe, $CoSe_2$, and SnSe) are considered to be promising anode materials. Besides their high theoretical capacity, metallic selenides have higher electrical conductivity, weaker metal-selenium bonds, narrower energy gaps, and larger lithium-insertion interstitial sizes than metallic oxides and sulfides, which accelerate the electron migration and the conversion reaction kinetics [11, 12]. However, metallic selenides still suffer from huge volume changes, particle aggregation, and relatively low intrinsic conductivities during charge/discharge processes [13].

Downsizing the metallic selenide to the nanoscale, complexing with conductive porous carbon, and doping engineering are effective routes to address the above issues [14]. In addition to the graphitic carbon nanosheets or organic molecules derived carbon [15–17], zeolitic imidazolate frameworks (ZIFs), a subclass of MOFs, derived composites have a unique porous structure with high specific surface area and uniform N doping, hence ZIFs derived metallic compounds/N doped porous carbon composites have been intensively investigated for LIBs and SIBs [18–21]. In particular, compared to mono metal compounds, the heterostructured electrodes with two metal compounds have a strong synergistic effect

between the different components at the interface, achieving higher electrical/ionic conductivities and lower activation energy, accelerating the reaction kinetics, and thus conducting the electrochemical performance [22–27]. For example, $In_2Se_3/CoSe_2$ hollow nanorods derived from the in situ gaseous selenization of ZIF-67 that grown on the surface of In-based MOF (MIL-68) [22], and CoSe@N-doped carbon anchored onto graphene with modified $MoSe_2$ nanosheets were prepared by a self-template and subsequent selenization strategy [23]. Core-shell ZIF-8@ZIF-67 precursors derived hybrids have closely packed double shells, in which the ZIF-8-derived inner shell act as the nanostructured hollow framework to facilitate the diffusion kinetics while the ZIF-67-derived outer shell has a stable structure and good conductivity, and phase boundary of heterogeneous $ZnSe/CoSe_x$ can be constructed [28].

In addition, constructing one-dimensional (1D) MOFs-derived architectures can further enhance the energy storage performance due to the unique structural advantages. Compared to the 0D structures, the 1D porous nanotubes have several advantages for electrochemical performance, such as their confined dimensions and can maintain electron transport along the long axis. Besides, the 1D porous structure not only buffers the expansion/contraction of the electrode but also depresses particle agglomeration during the charge/discharge process and improves the structural integrity. Moreover, the high surface area of the porous nanotube can make sufficient contact between active material and electrolyte. Therefore, the construction of well-aligned 1D structures from MOFs is of great importance for energy-related applications. [29–32]. Our group has confirmed the 1D ZIFs-derived nanocomposites prepared via electrospinning have higher structural stability and conductivity than the 0D derivatives, resulting from the assembly effect of electrospinning that can endow materials with enhanced or novel performance [33–35].

Inspired by the above analysis, we report a well-designed procedure to synthesize hierarchical architectures composed of ZnSe/CoSe nanodots (NDs) anchored porous carbon nanotubes (CNTs) coated by a graphitic carbon shell (ZnSe@CoSe@CN). Facilitating by the synergistic effect of the structure and component, combined with the assembly effect of electrospinning, the as-synthesized ZnSe@CoSe@CN NT delivers a high reversible capacity, excellent rate capability, and long-term cycling performance as a bifunctional anode for lithium and sodium storage.

2. Materials And Methods

Materials

All chemicals were purchased from Sinopharm Chemical Reagent Co., Ltd and were used without further treatment.

Synthesis of PAN@ZIF-8

0.8 g of zinc acetate dihydrate and 0.8 g of polyacrylonitrile (PAN) were separately dissolved in 10 mL of N, N-dimethylformamide (DMF), and the solution was electrospun with a flow rate of 0.3 mL/h, a high DC voltage of 11 kV, and an electrospun distance of 15 cm. After continuous spinning, the PAN fibrous film

containing Zn^{2+} could be stripped (PAN-$Zn(CH_3COO)_2$). Then, 3.25 g of 2-methylimidazole (2-MIA) was dissolved in 50 mL of ethanol, and then 80 mg of PAN-$Zn(CH_3COO)_2$ was immersed in the solution and maintained at 60°C for 3 h. Finally, the electrospun film was washed with ethanol several times and vacuum drying at 60°C overnight, obtaining PAN@ZIF-8 fibrous film.

Synthesis of PAN@ZIF-8@ZIF-67 and ZIF-8@ZIF-67

The PAN@ZIF-8 fibrous film was placed in 100 mL of a methanol solution containing 0.75 g of cobalt nitrate hexahydrate and 1.125 g of 2-MIA and maintained at 60°C for 5 h. The film was then methanol washed 3 times and vacuum dried at 60°C for 24 h to obtain PAN@ZIF-8@ZIF-67, and obtain ZIF-8@ZIF-67 nanotubes (NTs) after etching PAN in DMF overnight.

Synthesis of ZnSe@CoSe

The above obtained ZIF-8@ZIF-67 NTs and Se powders were mixed with a weight ratio of 1:1.5, and the mixture was annealed in an Ar atmosphere at a heating rate of 3°C min^{-1} and maintained at 650°C for 3 h, obtaining ZnSe and CoSe encapsulated N-doped porous CNTs (ZnSe@CoSe).

Synthesis of ZnSe@CoSe@CN

In order to get the target product ZnSe@CoSe@CN, 40 mg of ZnSe@CoSe and 20 mg of dopamine hydrochloride were dissolved in 100 mL of Tris HCl buffer solution (pH = 8.5) and stirred for 24 h. Then, the composite was centrifuged twice with water and ethanol and was dried in a vacuum drying oven at 70°C for 12 h. Finally, the obtained composite was calcined at 500°C for 4 h in an Ar atmosphere to obtain the target product of ZnSe@CoSe@CN.

For the contrast samples, the ZnSe@CN and CoSe@CN NTs were prepared in the same process as ZnSe@CoSe@CN, but derived from ZIF-8 and ZIF-67 NTs, respectively, while the Zn@Co@CN NTs were prepared via direct carbonization of ZIF-8@ZIF-67 without the selenization process.

Characterization

Scanning electron microscopy (SEM, Zeiss Supra 40, 5 kV), transmission electron microscope (TEM, Hitachi H7700, 100 kV), and high-resolution TEM (HRTEM, JEM-ARM 2100F Atomic Resolution Analytical Microscope, 200 kV) equipped with energy-dispersive X-ray spectroscopy (EDS) were used to investigate the morphology and microstructure of the material. The powder X-ray diffraction (PXRD) was characterized by the X-ray diffractometer (X' Pert PRO MPD) with Cu Kα radiation (k = 1.5406 Å). The X-ray photoelectron spectrometer (XPS) patterns were measured with an excitation source of Al Kα radiation (ESCALAB250Xi). Raman spectra were examined on a LABRAM-HR confocal laser micro Raman spectrometer. N_2 sorption analysis was conducted on an ASAP 2020 accelerated surface area and porosimetry instrument (Micromeritics) equipped with the automated surface area. Pore volume and size

analysis were obtained by Brunaure-Emmett-Teller (BET) calculations based on the Barrett-Joyner-Halenda (BJH) model.

Electrocatalytic measurements

The as-synthesized samples were applied as bifunctional anode materials for half lithium-ion battery (LIB) and sodium-ion battery (SIB). The active material, acetylene black, and PVDF were grinded into a uniform slurry according to a mass ratio of 7:2:1, and the slurry was evenly coated on a previously cleaned copper foil and dried in a vacuum drying oven at 60°C for 12 h. Then, the copper foil was cut into circular slices with a diameter of 12 mm and was used as a working electrode containing 0.8-1.0 mg cm^{-2} active substances with a thickness of ~ 0.2 mm. The batteries were assembled in a glove box filled with Ar and have the same electrolyte of 1 M $LiPF_6$ ethyl carbonate/dimethyl carbonate (1:1 w/w) solution, while using the lithium and sodium sheet as the counter electrode for LIB and SIB, respectively. The encapsulated batteries were left at room temperature for 24 h, and the constant current charge/discharge cycles were tested on a LAND test system with different current densities (0.1, 0.5, 1.0, 2.0, and 5.0 A g^{-1}) and a voltage test range of 0.01-3.0 V. The CV tests were tested with a test speed of 0.1 mV s^{-1} at 0.01-3.0 V on an Arbin electrochemical workstation. The electrochemical impedance spectroscopy test (EIS) was carried out via the CHI-760 electrochemical workstation measurement with a test frequency of 0.1-100000 Hz. The galvanostatic intermittent titration technique (GITT) profiles were tested with a titration time of 30 min and a rest time of 5 min at 0.1 A g^{-1}. The diffusion coefficient of Li^+ (D_{Li}+) in the ZnSe@CoSe@CN anode was determined according to the following equation:

$$D_{Li^+} = \frac{4}{\pi\tau}\left(\frac{m_B V_M}{M_B A}\right)^2\left(\frac{\Delta E_s}{\Delta E_\tau}\right)$$

in which the τ, ΔE_S, and $\Delta E\tau$ are the galvanic titration, voltage change between steps, and voltage change during the pulse period, respectively. Similarly to the D_{Na}+ calculation.

3. Results And Discussion

3.1 Material Synthesis and Characterization

The synthetic procedure for hierarchically porous N-doped CNTs encapsulated with ZnSe/CoSe nanodots (NDs) (ZnSe@CoSe@CN) is illustrated in Fig. 1a. First, the electrospun polyacrylonitrile (PAN) nanofibers containing zinc acetate (PAN@Zn($CH_3COO)_2$) were immersed in 2-methylimidazole methanol solution to form ZIF-8 crystals on the fiber surfaces (PAN@ZIF-8). The scanning electron microscopy (SEM) image shows a rough fiber surface of PAN@ZIF-8, and the fiber diameter increased from ~ 320 to ~ 390 nm, indicating the formed ZIF-8 layer has a thickness of ~ 70 nm (Fig. S1a-b). Second, a ZIF-67 layer was grown on the PAN@ZIF-8 surfaces via a facile solution reaction method (PAN@ZIF-8@ZIF-67), which had

no obvious morphology change but a larger diameter of ~ 480 nm, suggesting a ~ 90 nm thickness for the ZIF-67 layer (Fig. S1c). After solvent etching of PAN, the core-shell structured ZIF-8@ZIF-67 NTs were constructed (Fig. S2a-c) and were further calcined withSe powder under H_2/Ar. During the selenization process, H_2Se gas was first generated from combining H_2 with Se vapor and then reacted with the Zn/Co ions released from ZIF-8@ZIF-67 [35], developing abundant uniformly distributed ultrathin ZnSe and CoSe crystals, and the organic ligands in ZIFs were simultaneously carbonized to N-doped carbon, resulting in the formation of ZnSe and CoSe NDs anchored N-doped porous CNTs (ZnSe@CoSe) (Fig. S2b-d). Finally, to further enhance the structural stability and reversible capacity, a polydopamine (PDA) carbonized N-doped carbon layer was coated on the ZnSe@CoSe surface, and obtaining the ZnSe/CoSe doped hierarchical porous CNTs (ZnSe@CoSe@CN).

As indicated by the SEM and transmission electron microscope (TEM) images (Fig. 1b-c), the ZnSe@CoSe@CN nanocomposite has an obvious tubular structure anchored with lots of ultrathin black dots with a diameter of 5–15 nm, which are the ZnSe and CoSe NDs. The powder X-ray diffraction (XRD) pattern of ZnSe@CoSe@CN clearly shows the diffraction peaks of ZnSe (JCPDS No. 88-2345) and CoSe (JCPDS No. 89-2004), confirming the successful synthesis of ZnSe/CoSe crystals in the composite CNTs (Fig. 1d). The high-resolution TEM (HRTEM) image shows the nanodots are closely connected and form relatively large nanoparticles (Fig. 1e and Fig. S3). The crystal lattice spacing of 0.56, 0.32, 0.28, 0.20, and 0.17 nm correspond to the (100), (111), (200), (220), and (311) planes of ZnSe, respectively, while the lattice spacing of 0.202 and 0.27 nm corresponds to the (102) and (101) planes of CoSe [36]. In particular, besides the interfaces between the same component, abound of CoSe/ZnSe heterogeneous interfaces are constructed, and the obvious defects in the interface can generate a large number of active sites, which can enhance the electronic/ionic transmission and reaction kinetics, thus favoring the heterostructured electrodes with much enhanced electrochemical performances [37]. Moreover, graphitic carbon that can promote the conductivity and structural stability is observed in the composite CNTs, including those coated on the ZnSe/CoSe nanocrystals, randomly distributed in the amorphous carbon, and anchored on the composite surface derived from PDA. The selected area electron diffraction (SADE) patterns of ZnSe@CoSe@CN displayed the diffraction rings of crystalline ZnSe and CoSe (Fig. 1f), and the element mapping images show the uniformly dispersed C, N, O, Zn, Co, and Se elements in ZnSe@CoSe@CN (Fig. 1g), further indicating the successful selenization of ZIF-8 and ZIF-67.

Besides, several contrast samples were prepared to confirm the unique structural and component characters of ZnSe@CoSe@CN. The ZnSe@CN and CoSe@CN composites were prepared in the same process as ZnSe@CoSe@CN, but derived from ZIF-8 and ZIF-67 NTs, respectively. The Zn@Co@CN composite was constructed via direct carbonization of ZIF-8@ZIF-67 without the selenization process, while ZnSe@CoSe was prepared without PDA. These contrast samples show obvious tubular structures (Fig. S4), and the XRD patterns indicate the successful synthesis of CoSe and/or ZnSe crystals in the composites (Fig. S5a). In addition, the Raman spectra show the characteristic D- and G-bonds of carbon, which is related to the graphitic and disordered/defective carbon, respectively. ZnSe@CoSe@CN shows the lowest I_D/I_G value of 1.08, while ZnSe@CoSe has the highest I_D/I_G value of 1.18, indicating the PDA-

derived N-doped carbon layer favors increasing the graphitic degree, which is conducive to the electrochemical performance (Fig. S5b).

The chemical composition and valence states of the samples were studied by X-ray photoelectron spectroscopy (XPS) (Fig. 2a-f, Fig. S6 and Table S1). The total spectrum of ZnSe@CoSe@CN indicates a close result with the elemental mapping analysis (Fig. 2a). The peaks at 284.7, 286.2, and 288.1 eV in the high-resolution C 1s spectrum represent C-C/C = C, C = N, and C-O bonds, respectively (Fig. 2b). The N 1s spectrum can be deconvolved into three peaks of 398.4, 399.8, and 401.5 eV, corresponding to pyridine-N, pyrrole-N, and graphite-N, respectively (Fig. 2c), and the schematic bonding structure of the three types of N dopants is shown in Fig. 2h. These N dopants can introduce surface defects and bond directly with metal atoms and graphitic carbon, thus producing multiple channels for Li^+/Na^+ diffusion and strengthening the coupling effect between carbon and metal atoms, which are beneficial to improving the performance of the battery. In the Zn 2p spectrum (Fig. 2d), the peaks located at 1022.2 and 1045.1 eV correspond to Zn $2p_{3/2}$ and Zn $2p_{1/2}$ of ZnSe [38]. There are two spin-orbit peaks for $2p_{3/2}$ (780.88 eV) and $2p_{1/2}$ (797.18 eV) in the Co 2p spectrum (Fig. 2e), in which the Co-Se-Co bond at 780.1 eV, the Co-N bond at 782.5 eV, the shake-up satellites of Co 2p at 786.1 and 803.7 eV that resulting from the antibonding orbital between Co and Se atoms can be revealed. Specifically, the peaks at 781.1 and 797.2 eV correspond to Co-O, which may be due to partial surface oxidation [39]. Five peaks can be identified in the Se 3d and Co 3p spectrum (Fig. 2f), including the Se $3d_{5/2}$ at 54.7 eV, the Se $3d_{3/2}$ at 55.8 eV can be assigned to the Se-Se and Co-Se, the Se-C/O bond at 58.5 eV, the Co $3p_{1/2}$ bond at 59.1 eV, and the SeO_2 at 61.3 eV [40]. It should be noted that compared to ZnSe@CoSe@CN, ZnSe@CN has lower Zn $2p_{1/2}$ and Zn $2p_{3/2}$ peaks of 1045.03 and 1022.03 eV (Fig. S6e), and CoSe@CN also shows lower Co $2p_{1/2}$ and Co $2p_{3/2}$ peaks of 796.58 and 778.68 eV (Fig. S6f). The Zn 2p and Co 2p peaks of ZnSe@CoSe@CN migrated to higher binding energy, resulting from the lattice distortion and defects at the two-phase boundary. These binding energy migrations could accelerate the electron movement from ZnSe to CoSe for charge compensation, resulting in increased electron density of CoSe that give rise to Li^+/Na^+ absorption and reaction kinetics improvement [23, 41].

The porous structure characterized by the N_2 sorption isotherm shows an IV-type curve with an evident hysteresis loop (Fig. 2g and Fig. S7), indicating the as-synthesized samples have a mesoporous structure with a similar pore size distribution, and the pore size centered at ~ 0.5 nm suggests the samples also have a microporous structure. Among the samples, Zn@Co@CN has the highest specific Brunauer–Emmett–Teller (BET) surface area of 275.49 $m^2 \cdot g^{-1}$ and the largest total pore volume of 5.693 $cm^3 \cdot g^{-1}$. Although the selenidation process may decrease the BET surface area and pore volume, ZnSe@CoSe@CN has a high specific BET surface area of 191.267 $m^2 \cdot g^{-1}$, which is higher than the samples of ZnSe@CN, CoSe@CN, and ZnSe@CoSe, confirming the core-shell ZIF-8@ZIF-67 precursor and the CN coating layer are conductive to increase the specific surface area. Besides, the ZnSe@CoSe@CN NT also has a large total pore volume of 4.454 $cm^3 \cdot g^{-1}$, which is beneficial to the contact between active

materials and electrolytes, shortening the Li^+/Na^+ diffusion pathways and relieving the inevitable volume change of ZnSe/CoSe during the charge/discharge process (Table S2) [42–44].

The electrochemical performance of the as-prepared hierarchical composite NTs was investigated as the anode material for LIBs. As illustrated in the typical cyclic voltammetry (CV) curves of the ZnSe@CoSe@CN anode (Fig. S8a), the cathodic peak at 1.27 V can be related to the Li^+ insertion and formation of Li_xCoSe (CoSe → Li_xCoSe). The peak at 0.69 V corresponds to the formation of solid electrolyte interface (SEI) films and the conversion reaction of Li_xCoSe to Li_2Se and metallic Co (CoSe → Co + Li_2Se), and the peak at 0.56 V corresponds to the solid electrolyte interface (SEI) layer formation and the reduction of ZnSe (ZnSe → Li_2Se + Zn → Li_2Se + Li_xZn → Li_2Se + LiZn). Correspondingly, the oxidation peak at 1.36 V in the first charge process is ascribed to the multi-step dealloying reaction of Li_xZn alloy phase and the oxidation of LiZn to ZnSe, and the broad oxidation peak at 2.09 V can be assigned to the reversible selenization of Co to CoSe (Co + Li_2Se → Li_xCoSe → CoSe) [40]. During the second cycle, the reduction peaks shift to 1.41 V and a broad peak of 0.91 V, and the oxidation peaks remain unchanged. The peak position change may result from the irreversible side reactions and activation processes caused by the initial lithium insertion/desorption in the first cycle. The following scan showed maintained CV curves, suggesting that the conversion process of ZnSe@CoSe@CN is highly reversible and stable. ZnSe@CN and CoSe@CN displayed the corresponding CV curves, demonstrating the above-mentioned mechanism analysis is reasonable (Fig. S8b-e). Moreover, the galvanostatic discharge/charge (GDC) curve of the first discharge process revealed two obvious platforms at 1.25 and 0.56 V, in which the former was attributed to the lithiation of CoSe while the latter was the lithiation of ZnSe and the formation of SEI film. For the first charge process, the platform at 1.36 and 2.0-2.5 V can be attributed to the formation of ZnSe and CoSe, respectively, consistent with the electrochemical reaction at the corresponding peak position in the CV curve. ZnSe@CoSe@CN delivered high initial discharge/charge capacities of 2739 and 1583 mAh g^{-1}, respectively, with an initial coulombic efficiency (CE) of 57.79%, the low CE may be caused by the SEI films formation and irreversible decomposition of the electrolyte [45]. In particular, the discharge capacity can be conserved at 1500 mAh g^{-1} after 100 cycles (Fig. 3a), much higher than the other contrast samples (Fig. S9). The high lithium storage performance confirms the unique component and structural advantages of ZnSe@CoSe@CN.

The rate performance of the as-prepared electrodes is further investigated (Fig. 3b). Compared to the contrast electrodes, ZnSe@CoSe@CN shows the highest capacity of 1216.2, 1032.8, 960.4, 891.8, 807.6, and 708.1 mAh g^{-1} at 0.1, 0.2, 0.5, 1, 2, and 3 A g^{-1}, respectively, and a high capacity of 650.8 mAh g^{-1} can be delivered even at an ultrahigh current density of 5 A g^{-1}. More importantly, the capacity can be maintained at 1230 mAh g^{-1} when the current density is back to 0.1 A g^{-1}, confirming a high reversible rate capability. The striking rate performance of ZnSe@CoSe@CN results from the rapid Li^+ diffusion through the ZnSe and CoSe interlayers, and the conductive 1D porous structure promoted Li^+ diffusion kinetics.

Long-term cyclic stability is another required feature for ideal anodes in LIBs. During the first several cycles at 0.1 A g^{-1}, all of the samples displayed decreased capacity and enlarged CE (Fig. 3c). After that, the anodes show steady capacity. ZnSe@CoSe@CN exhibited a high capacity of 1595.8 mAh g^{-1} after 100 cycles, considerably higher than that of ZnSe@CN (919.4 mAh g^{-1}), CoSe@CN (1178.1 mAh g^{-1}), Zn@Co@CN (1189.6 mAh g^{-1}), and ZnSe@CoSe (884.8 mAh g^{-1}). Besides, the ZnSe@CoSe@CN anode still exhibited the highest capacity of 1087.4 mAh g^{-1} after 200 cycles at 1 A g^{-1} and 813.7 mAh g^{-1} after 400 cycles at 2 A g^{-1}, respectively (Fig. S10). Particularly, a remarkable capacity of 600 mAh g^{-1} was maintained even after 1000 cycles at 5 A g^{-1}, while ZnSe@CoSe cannot maintain 300 cycles at this high current density because the structure collapsed during the cyclic process, further indicating the importance of the PDA-derived carbon layer on structural stability (Fig. 3d) These results confirm the superior long-term cyclic stability of ZnSe@CoSe@CN. It should be noted that the ZnSe@CoSe@CN anode prepared in this work is also among the best anodes based on the comparison with other reported metal selenide-based anodes for LIBs (Fig. 3e and Table S3) [36, 45–51].

According to the previous reports, the corresponding electrode storage mechanism can be revealed according to the relationship between peak current (i) and scan rate (v): $i = a v^b$, in which the calculated b value of 0.5 and 1.0 indicate the electrochemical reaction is dominantly through diffusion behavior and pseudo-capacitive behavior, respectively [46]. In this work, the CV curves were tested at different scan rates from 0.2 to 1.0 mV s^{-1} (Fig. 4a), the fitted b-values of recurring peak 1 to peak 4 for ZnSe@CoSe@CN are 0.98, 0.759, 0.847, and 0.786, respectively (Fig. 4b), confirming a pseudo-capacitive dominant behavior during the redox process. The capacity contribution ratio can be calculated by the following equation: $i = k_1 v + k_2 v^{1/2}$, where $k_1 v$ and $k_2 v^{1/2}$ correspond to the capacity and diffusion contributions. The calculated capacity contribution is increased from 70.52% at 0.2 mV s^{-1} to 83.84% at 1 mV s^{-1} (Fig. 4c-d), further indicating a pseudo-capacitance dominant process in the whole lithium storage capacity, which benefits the lithium storage performance [48].

Furthermore, the diffusion coefficient of Li^+ ($D_{Li}+$) in the ZnSe@CoSe@CN anode upon the lithiation and delithiation process was measured by the galvanostatic intermittent titration technique (GITT), which suggests fast Li^+ diffusion kinetics (Fig. 4e-f). The $D_{Li}+$ value range of ZnSe@CoSe@CN in the discharging and charging process is 3.12×10^{-14} to 6.29×10^{-13} and 5.31×10^{-14} to 6.97×10^{-13}, respectively, indicating a good diffusion ability. This should attribute to the ZnSe/CoSe phase interface generated lattice defects leading to the fast Li^+ migration and storage, and the hierarchical porous tubular structure assists sufficient contact of electrolyte and electron transport, resulting in the high pseudo-capacitive contribution and the minimal charge transfer resistance of ZnSe@CoSe@CN. As indicated by the Nyquist plots measured via the electrochemical impedance spectroscopy (EIS), ZnSe@CoSe@CN has a R_e value of 4.43 Ω and R_{ct} value of 115.70 Ω, which are the lowest resistance among the as-prepared samples (Fig. 4g), suggesting a much fast ion diffusion and reaction kinetics, hence superior rate performance [50]. Therefore, the construction of heterostructured bimetallic selenides within the hierarchical porous CNTs is conducive to improving the pseudo-capacitive contribution, fasting the

electron transfer rate and reaction kinetics, and finally to the enhancement of the electrochemical performance.

Meanwhile, the reaction mechanism of ZnSe@CoSe@CN was analyzed via ex-situ XRD tests. As shown in the ex-situ XRD patterns with corresponding discharge and charge voltages (Fig. 4h-i), during the discharge process from stage A to stage B, the ZnSe phase can still be detected, while the strength of the CoSe phase decreases significantly, and the signals of Co and Li_2Se can be observed, indicating that CoSe has experienced the insertion of Li^+ at a higher potential than the ZnSe phase. When further discharging to 0.01 V (stage D), the peaks of ZnSe and CoSe phases disappear, while the signals of Co, Zn, and Li_2Se become obvious, indicating that both ZnSe and CoSe have gone through a complete lithification process except the alloying reaction between Li and Zn/Co. Besides, the broad peak centered at 24° is the amorphous and the graphitic plane (002) of carbon [35]. During the delithiation process, when the electrode is charged to 0.75 V (stage E), the ZnSe signal can be clearly observed and CoSe signals appear in weak intensity, while the Co and Li_2Se phases still exist, indicating ZnSe experienced the Li^+ intercalation process, while CoSe only observed part of lithium intercalation. In the fully charged state (stage G), the Li_2Se phase disappears, and the ZnSe and CoSe phases can be detected, indicating that both ZnSe and CoSe phases have gone through the complete delithiation reformulation process and returned to the initial state, further confirming the high reversibility of the ZnSe@CoSe@CN anode.

Moreover, the SEM and TEM images of the ZnSe@CoSe@CN anode after 200 cycles at 1 A g^{-1} show the obvious 1D porous morphology, the HRTEM image and XRD pattern indicate the existence of ZnSe and CoSe crystals, and the EDX spectrum and element mapping images confirm the existence and even distribution of the elements (Fig. S11), indicating the high structural integrity of ZnSe@CoSe@CN.

The sodium storage performance also has been investigated to further confirm the structural and composition advantages of the hierarchical porous ZnSe@CoSe@CN NTs. The CV curves tested at 0.1 mV s^{-1} within 0.01-3 V revealed the electrochemical reaction details (Fig. S12). Taking ZnSe@CoSe@CN as an example, in the first cathodic scan, the peaks at around 0.51, 1.19, and 1.48 V are related to the SEI film formation and Na^+ insertion into CoSe to form Na_xCoSe, and the reduction of Na_xCoSe to Co and Na_2Se processes ($CoSe \rightarrow Na_xCoSe \rightarrow Co + Na_2Se$) [52]. The reduction peak at 0.38 V is corresponded to the conversion reaction between ZnSe and Na to form Zn and Na_2Se ($ZnSe \rightarrow Zn + Na_2Se$), and the peak at 0.05 V is attributed to the formation of alloying $NaZn_{13}$ [53]. For the first anodic scan, the distinct peak at 1.03 V is due to the removal of Na^+ and conversion reaction of Zn to ZnSe, and the peaks of 1.51 and 1.77 V are ascribed to the multistep electrochemical reaction between Co and Na_2Se to form CoSe [38, 40]. The CV curves overlap well from the second cycle, suggesting high reaction reversibility. The plateaus in the GDC profile correspond to the peaks in the CV curves, and there is no significant difference in the subsequent cycles, further confirming the excellent repeatability of ZnSe@CoSe@CN (Fig. 5a). The first discharge and charge capacities of ZnSe@CoSe@CN are 660 and 559 mAh g^{-1}, respectively, with a CE value of 84.6%. In sharp contrast, the control samples deliver much lower repeatability and charge/discharge capacities (Fig. S13).

The prepared tubular ZnSe@CoSe@CN anode exhibits excellent rate capability, a surprisingly reversible capacity of 523.2, 501.3, 481.2, 457.9, 423.1, 396.4, and 331 mAh g^{-1} can be retained when the current density is 0.1, 0.2, 0.5, 1.0, 2.0, 3.0, and 5.0 A g^{-1} (Fig. 5b), respectively, and the capacity can be recovered to 515 mAh g^{-1} when the current density is returned to 0.1 A g^{-1}, higher than the contrast samples, suggesting the unique structure and component advantages of ZnSe@CoSe@CN for Na^+ insertion and desertion. Moreover, the ZnSe@CoSe@CN anode exhibits superior long-term cycling stability, a reversible capacity of 622.3 mAh g^{-1} after 100 cycles at 0.1 A g^{-1} can be maintained (Fig. 5c), which is much higher than ZnSe@CN (329.7 mAh g^{-1}), CoSe@CN (312.8 mAh g^{-1}), Zn@Co@CN (237.2 mAh g^{-1}), and ZnSe@CoSe (212.8 mAh g^{-1}). Meanwhile, a considerable capacity of 429.6 and 397.1 mAh g^{-1} can be maintained after 200 cycles at 1 A g^{-1} and 400 cycles at 2 A g^{-1}, respectively (Fig. S13), even achieving a high capacity of 397.3 mAh g^{-1} after 1000 cycles at 5 A g^{-1} (Fig. 5d). ZnSe@CoSe@CN is among the best selenide-based anode materials for SIBs (Fig. 5e and Table S4) [37, 39, 53–59].

To interpret the high-rate capability, the electrochemical kinetics of the ZnSe@CoSe@CN anode was investigated by a series of measurements at 0.2 ~ 1.0 mV s^{-1} (Fig. 6). The CV curves present similar shapes at different scan rates of 0.2-1.0 mV s^{-1}, and have quantified b-values of 0.87, 0.95, 0.98, 0.97, and 0.87 for anodic and cathodic peaks, indicating a capacitive dominant characteristic of ZnSe@CoSe@CN (Fig. 6a-d). As shown in Fig. 6c, a dominant capacitive contribution of 93.62% can be quantified in the CV curve at 1.0 mV s^{-1}. As the scan rate decreases, the capacitive contribution further decreases to a minimum value of 86.54% at 0.2 mV s^{-1} (Fig. 6d).

The GITT curve indicates a high calculated diffusion coefficient of Na^+ (D_{Na}+) values of 2.19×10^{-14} ~ 6.62×10^{-13} and 5.81×10^{-14} ~ 6.77×10^{-13} during the discharging/charging process for ZnSe@CoSe@CN (Fig. 6e-f), indicating fast reaction kinetics. As indicated by the EIS spectra, the ZnSe@CoSe@CN anode has the lowest R_e value of 5.79 Ω and R_{ct} value of 37.91 Ω among the as-prepared samples (Fig. 6g), which is in agreement with the GITT results. These results suggest that in addition to Li^+, the unique 1D hierarchical porous tubular architecture anchored with heterostructured bimetallic selenides also has a high Na^+ diffusion ability, benefiting the high capacitance contribution of ZnSe@CoSe@CN, which efficiently enhance the cycling and rate capability for SIB. In addition, the possible reaction mechanism of ZnSe@CoSe@CN for SIBs anode was also analyzed by ex-situ XRD tests. As shown in the ex-situ XRD patterns with corresponding discharge and charge voltages (Fig. 6i-h), during the discharge process, the CoSe and ZnSe diffraction peaks gradually disappeared and new peaks appear that correspond to Na_2Se, Co, and $NaZn_{13}$. During the desertion process, the CoSe and ZnSe peaks reappeared, indicating the high reversibility of the ZnSe@CoSe@CN anode.

The remarkable lithium/sodium storage performance could be attributed to the electrospinning-assisted assembly effect on the 1D hierarchical porous tubular architecture, in which the hollow porous structure can accommodate the volume expansion generated during the conversion reaction, which is beneficial to preserving the structural stability of the anode. Besides, the porous structure with a thin wall and high

specific surface area accelerates the Li^+/Na^+ insertion/desertion ability and favors the contact with electrolytes. Also, downsizing ZnSe and CoSe to nanoscale effectively reduces the Li^+/Na^+ diffusion distance and the mechanical stress during the charging/discharging process, and the heterogeneous phase interface with lattice defects accelerates the electrons transportation and the diffusion rate of Li^+ and Na^+, hence the tubular ZnSe@CoSe@CN composite exhibits fast reaction kinetics. Moreover, the PDA-derive N-doped carbon coating layer prevents pulverization and increases the conductivity of the material, further enhancing the structure stability and lithium/sodium storage performance.

Conclusion

In summary, core-shell MOFs-derived hierarchically porous N-doped CNTs anchored with ultrafine ZnSe/CoSe NDs (ZnSe@CoSe@CN) have been rational designed and prepared as excellent bifunctional anode material for lithium and sodium storage. The ZnSe@CoSe@CN anode delivers a high rate capability and cycling stability, a high reversible capacity of 1500 and 622.3 mAh g^{-1} at 100 mA g^{-1} after 100 cycles, and 600 and 397.3 mAh g^{-1} at 5000 mA g^{-1} after 1000 cycles can be maintained for LIB and SIB, respectively. This work provides an effective strategy for engineering microstructures to exploit high-performance anode for LIBs and SIBs.

Declarations

Conflicts of interest: The authors declare no competing financial interest.

Acknowledgements

We acknowledge the funding support from the NSAF Joint Fund (Grant U1930112), the Fundamental Research Funds for the Central Universities (PA2021KCPY0042, JZ2022HGTB0240), and the Anhui Provincial Natural Science Foundation (1908085ME155).

Appendix A. Supplementary data

Supplementary data associated with this article can be found in the online version at XXX.

Author contributions statement

Chuan-Ling Zhang designed and guided the experiments and wrote the manuscript, Qiang Zhang, Meng-Li Chen, Xi-Xi Zhu, and Chen-Fan Zhao did the experiments, Fu-Hu Cao and Hao Li analyzed the data and revised the manuscript, and Huai-Ping Cong revised the figures and manuscript. All authors reviewed the manuscript.

References

1. Hwang JY, Myung ST, Sun YK (2017) Sodium-ion batteries: present and future. Chem Soc Rev 46:3529–3614.

2. Zhang L, Wang H, Zhang X, Tang Y (2021) A Review of Emerging Dual-Ion Batteries: Fundamentals and Recent Advances. Adv Funct Mater 31:2010958.
3. Wang G, Yu M, Feng X (2021) Carbon materials for ion-intercalation involved rechargeable battery technologies. Chem Soc Rev 50:2388–2443.
4. Turcheniuk K, Bondarev D, Singhal V, Yushin G (2018) Ten years left to redesign lithium-ion batteries. Nature 559:467–470.
5. Delmas C (2018) Sodium and Sodium-Ion Batteries: 50 Years of Research. Adv Energy Mater 8:1703137.
6. Tan DHS, Banerjee A, Chen Z, Meng YS (2020) From nanoscale interface characterization to sustainable energy storage using all-solid-state batteries. Nat Nanotechnol 15:170–180.
7. Manthiram A (2020) A reflection on lithium-ion battery cathode chemistry. Nat Commun 11:2000804.
8. Pomerantseva E, Bonaccorso F, Feng X, Cui Y, Gogotsi Y (2019) Energy storage: The future enabled by nanomaterials. Science 366:969.
9. Wu F, Maier J, Yu Y (2020) Guidelines and trends for next-generation rechargeable lithium and lithium-ion batteries. Chem Soc Rev 49:1569–1614.
10. Cai KD, Jing XQ, Zhang YT, Li L, Lang XS (2022) A novel reed-leaves like aluminum-doped manganese oxide presetting sodium-ion constructed by coprecipitation method for high electrochemical performance sodium-ion battery. Int J Energy Res 46:14570–14580.
11. Chen M, Liu Y, Zhang Y, Xing G, Tang Y (2022) Lithium-rich sulfide/selenide cathodes for next-generation lithium-ion batteries: challenges and perspectives. Chem Commun 58:3591–3600.
12. Luo M, Yu H, Hu F, Liu T, Cheng X, Zheng R, Bai Y, Shui M, Shu J (2020) Metal selenides for high performance sodium ion batteries. Chem Eng J 380:122557.
13. Xiao X, Zou L, Pang H, Xu Q (2020) Synthesis of micro/nanoscaled metal-organic frameworks and their direct electrochemical applications. Chem Soc Rev 49:301–331.
14. Tabassum H, Zhi C, Hussain T, Qiu T, Aftab W, Zou R (2019) Encapsulating Trogtalite $CoSe_2$ Nanobuds into BCN Nanotubes as High Storage Capacity Sodium Ion Battery Anodes. Adv Energy Mater 9:1901778.
15. Indra A, Song T, Paik U (2018) Metal Organic Framework Derived Materials: Progress and Prospects for the Energy Conversion and Storage. Adv Mater 30:1705146.
16. Mu SN, Liu QR, Kidkhunthod P, Zhou XL, Wang WL, Tang YB (2021) Molecular grafting towards high-fraction active nanodots implanted in N-doped carbon for sodium dual-ion batteries [J]. Natl Sci Rev 8:nwaa178.
17. Liu P, Han J, Zhu K, Dong Z, Jiao L (2020) Heterostructure $SnSe_2$/ZnSe@PDA Nanobox for Stable and Highly Efficient Sodium-Ion Storage. Adv Energy Mater 10:2000741.
18. Dang S, Zhu QL, Xu Q (2017) Nanomaterials derived from metal–organic frameworks. Nat Rev Mater 3:17075.

19. Xu X, Liu J, Liu J, Ouyang L, Hu R, Wang H, Yang L, Zhu M (2018) A General Metal-Organic Framework (MOF)-Derived Selenidation Strategy for In Situ Carbon-Encapsulated Metal Selenides as High-Rate Anodes for Na-Ion Batteries. Adv Funct Mater 28:1707573.
20. Yang W, Li X, Li Y, Zhu R, Pang H (2019) Applications of Metal-Organic-Framework-Derived Carbon Materials. Adv Mater 31:1804740.
21. Yang J, Gao H, Men S, Shi Z, Lin Z, Kang X, Chen S (2018) $CoSe_2$ Nanoparticles Encapsulated by N-Doped Carbon Framework Intertwined with Carbon Nanotubes: High-Performance Dual-Role Anode Materials for Both Li- and Na-Ion Batteries. Adv Sci 5:1800763.
22. Xiao SH, Li XY, Zhang WS, Xiang Y, Li TS, Niu XB, Chen JS, Yan QY (2021) Bilateral Interfaces in In_2Se_3-$CoIn_2$-$CoSe_2$ Heterostructures for High-Rate Reversible Sodium Storage. ACS Nano 15:13307–13318.
23. Xu YN, Liu XF, Su H, Jiang S, Zhang JM, Li D (2022) Hierarchical Bimetallic Selenides $CoSe_2$-$MoSe_2$/rGO for Sodium/Potassium-Ion Batteries Anode: Insights into the Intercalation and Conversion Mechanism. Energy Environ Mater 5:627–636.
24. Zhang Y, Tao L, Xie C, Wang D, Zou Y, Chen R, Wang Y, Jia C, Wang S (2020) Defect Engineering on Electrode Materials for Rechargeable Batteries. Adv Mater 32:1905923.
25. Huang S, Wang Z, Von Lim Y, Wang Y, Li Y, Zhang D, Yang HY (2021) Recent Advances in Heterostructure Engineering for Lithium-Sulfur Batteries. Adv Energy Mater 11:2003689.
26. Li Y, Zhang J, Chen Q, Xia X, Chen M (2021) Emerging of Heterostructure Materials in Energy Storage: A Review. Adv Mater 33:2100855.
27. Pan QG, Tong ZP, Su YQ, Zheng YP, Shang L, Tang YB (2022) Flat-Zigzag Interface Design of Chalcogenide Heterostructure toward Ultralow Volume Expansion for High-Performance Potassium Storage. Adv Mater 34:2203485.
28. Liu JB, Lin CJ, Xie QS, Peng DL, Xie RJ (2022) Core-shell zeolite imidazole framework-derived ZnSe@$CoSe_2$/C heterostructure enabling robust polysulfide adsorption and rapid Li^+ diffusion in high-rate and high-loading lithium-sulfur batteries. Chem Eng J 430:133099.
29. Zhou G, Xu L, Hu G, Mai L, Cui Y (2019) Nanowires for Electrochemical Energy Storage. Chem Rev 119:11042–11109.
30. Wei QL, Xiong FY, Tan SS, Huang L, Lan EH, Dunn B, Mai LQ (2017) Porous One-Dimensional Nanomaterials: Design, Fabrication and Applications in Electrochemical Energy Storage. Adv Mater 29:1602300.
31. Wang C, Kaneti YV, Bando Y, Lin J, Liu C, Li J, Yamauchi Y (2018) Metal-organic framework-derived one-dimensional porous or hollow carbon-based nanofibers for energy storage and conversion. Mater Horiz 5:394–407.
32. Chen S, Qiu L, Cheng HM (2020) Carbon-Based Fibers for Advanced Electrochemical Energy Storage Devices. Chem Rev 120:2811–2878.

33. Zhang CL, Lu BR, Cao FH, Wu ZY, Zhang W, Cong HP, Yu SH (2019) Electrospun metal-organic framework nanoparticle fibers and their derived electrocatalysts for oxygen reduction reaction. Nano Energy 55:226–233.
34. Zhang CL, Jiang ZH, Lu BR, Liu JT, Cao FH, Li H, Yu ZL, Yu SH (2019) MoS_2 nanoplates assembled on electrospun polyacrylonitrile-metal organic framework-derived carbon fibers for lithium storage. Nano Energy 61:104–110.
35. Zhang CL, Liu JT, Li H, Qin L, Cao FH, Zhang W (2020) The controlled synthesis of Fe_3C/Co/N-doped hierarchically structured carbon nanotubes for enhanced electrocatalysis. Appl Catal B Environ 261:118224.
36. Park GD, Park JS, Kim JK, Kang YC (2022) Metal sulfoselenide solid solution embedded in porous hollow carbon nanospheres as effective anode material for potassium-ion batteries with long cycle life and enhanced rate performance. Chem Eng J 428:131051.
37. Liu HD, Lin Y, Li MN, Zhang L, Lu Y, Xiao W (2021) ZnSe/CoSe/NCDPH composites as anode materials for lithium ion batteries with high capacity and long cycle. Int J Hydrog Energy 46:30818–30827.
38. Yan WG, Cao MH, Fan SQ, Liu XH, Liu T, Li HS, Su J (2021) Multi-yolk ZnSe/2($CoSe_2$)@NC heterostructures confined in N-doped carbon shell for high-efficient sodium-ion storage. Compos Pt B-Eng 213:108732.
39. Li XY, Han ZY, Yang WH, Li Q, Li HS, Xu J, Li HL, Liu B, Zhao HG, Li SD, Wang X, Wu XL (2021) 3D Ordered Porous Hybrid of ZnSe/N-doped Carbon with Anomalously High Na^+ Mobility and Ultrathin Solid Electrolyte Interphase for Sodium-Ion Batteries. Adv Funct Mater 31:2106194.
40. Jiang Y, Xie M, Wu F, Ye Z, Zhang Y, Wang Z, Zhou Y, Li L, Chen R (2021) Cobalt Selenide Hollow Polyhedron Encapsulated in Graphene for High-Performance Lithium/Sodium Storage. Small 17:2102893.
41. Zhang Z, Huang Y, Liu XD, Wang X, Liu PB (2020) Core-Shell Co, Zn Bimetallic Selenide Embedded Nitrogen-Doped Carbon Polyhedral Frameworks Assist in Sodium-Ion Battery Ultralong Cycle. ACS Sustain Chem Eng 8:8381–8390.
42. Wu HB, Lou XW (2017) Metal-organic frameworks and their derived materials for electrochemical energy storage and conversion: Promises and challenges. Sci Adv 3:eaap9252.
43. Cao X, Tan C, Sindoro M, Zhang H (2017) Hybrid micro-/nano-structures derived from metal-organic frameworks: preparation and applications in energy storage and conversion. Chem Soc Rev 46:2660–2677.
44. Yang H, Wang X (2018) Secondary-Component Incorporated Hollow MOFs and Derivatives for Catalytic and Energy-Related Applications. Adv Mater e1800743-e1800743.
45. Jin J, Zheng Y, Kong LB, Srikanth N, Yan QY, Zhou KA (2018) A reflection on lithium-ion battery cathode chemistry. J Mater Chem A 6:15710–15717.

46. Zhang JL, Du CF, Zhao J, Ren H, Liang QH, Zheng Y, Madhavi S, Wang X, Zhu W, Yan QY (2018) $CoSe_2$-Decorated $NbSe_2$ Nanosheets Fabricated via Cation Exchange for Li Storage. ACS Appl Mater Interfaces 10:37773–37778.
47. Liu Q, Hou JG, Hao Q, Huang P, Xu CX, Zhou QX, Zhou J, Liu H (2020) Nitrogen-doped carbon encapsulated hollow ZnSe/$CoSe_2$ nanospheres as high performance anodes for lithium-ion batteries. Nanoscale 12:22778–22786.
48. Yang J, Gao HC, Men S, Shi ZQ, Lin Z, Kang XW, Chen SW (2018) $CoSe_2$ Nanoparticles Encapsulated by N-Doped Carbon Framework Intertwined with Carbon Nanotubes: High-Performance Dual-Role Anode Materials for Both Li- and Na-Ion Batteries. Adv Sci 5:1800763.
49. Ma DJ, Zhu QL, Li XT, Gao HC, Wang XF, Kang XW, Tian Y (2019) Unraveling the Impact of Ether and Carbonate Electrolytes on the Solid-Electrolyte Interface and the Electrochemical Performances of ZnSe@C Core-Shell Composites as Anodes of Lithium-Ion Batteries. ACS Appl Mater Interfaces 11:8009–8017.
50. Joshi B, Samuel E, Kim YI, Periyasami G, Rahaman M, Yoon SS (2021) Bimetallic zeolitic imidazolate framework-derived substrate-free anode with superior cyclability for high-capacity lithium-ion batteries. J Mater Sci Technol 67:116–126.
51. Zhang Z, Huang Y, Li X, Zhang S, Jia QX, Li TH (2021) Hollow carbon nanocages toward long cycle lifespan lithium/sodium-ion half/full batteries. Chem Eng J 421:129827.
52. Zhang X, He PJ, Dong BW, Mu N, Liu YG, Yang T, Mi RY (2021) Synthesis and characterization of metal-organic framework/biomass-derived CoSe/C@C hierarchical structures with excellent sodium storage performance. Nanoscale 13:4167–4176.
53. Shi NX, Chu YT, Xi BJ, Huang M, Chen WH, Duan B, Zhang CH, Feng JK, Xiong SL (2020) Sandwich Structures Constructed by ZnSe subset of N-C@$MoSe_{(2)}$ Located in Graphene for Efficient Sodium Storage. Adv Energy Mater 10:2002298.
54. Shi JW, Li H, Liu YW, Lu QY, Gao F (2022) Molybdenum Sulfide Selenide Nanosheets Synergized with Nitrogen-Rich Carbon Frameworks toward High Performance and Stable Sodium Storage. Adv Mater Interfaces 9:2102408.
55. Yousaf M, Chen YJ, Tabassum H, Wang ZP, Wang YS (2020) A Dual Protection System for Heterostructured 3D CNT/$CoSe_2$/C as High Areal Capacity Anode for Sodium Storage. Adv Sci 7:1902907.
56. Jeong SY, Cho JS (2019) Porous Hybrid Nanofibers Comprising ZnSe/$CoSe_2$/Carbon with Uniformly Distributed Pores as Anodes for High-Performance Sodium-Ion Batteries. Nanomaterials Basel 9:1362.
57. Yin, H.; Qu, H. Q.; Liu, Z. T.; Jiang, R. Z.; Li, C.; Zhu, M. Q (2019) Long cycle life and high rate capability of three dimensional $CoSe_2$ grain-attached carbon nanofibers for flexible sodium-ion batteries. Nano Energy 58:715–723.

58. Chen J, Pan AQ, Wang YP, Cao XX (2019) Hierarchical mesoporous $MoSe_2$@CoSe/N-doped carbon nanocomposite for sodium ion batteries and hydrogen evolution reaction applications. Energy Stor Mater 21:97–106.
59. Feng J, Luo SH, Yan SX, Zhan Y, Wang Q, Zhang YH, Liu X, Chang LJ (2021) Rational Design of Yolk-Shell Zn-Co-Se@N-Doped Dual Carbon Architectures as Long-Life and High-Rate Anodes for Half/Full Na-Ion Batteries. Small 17:2101887.

Figures

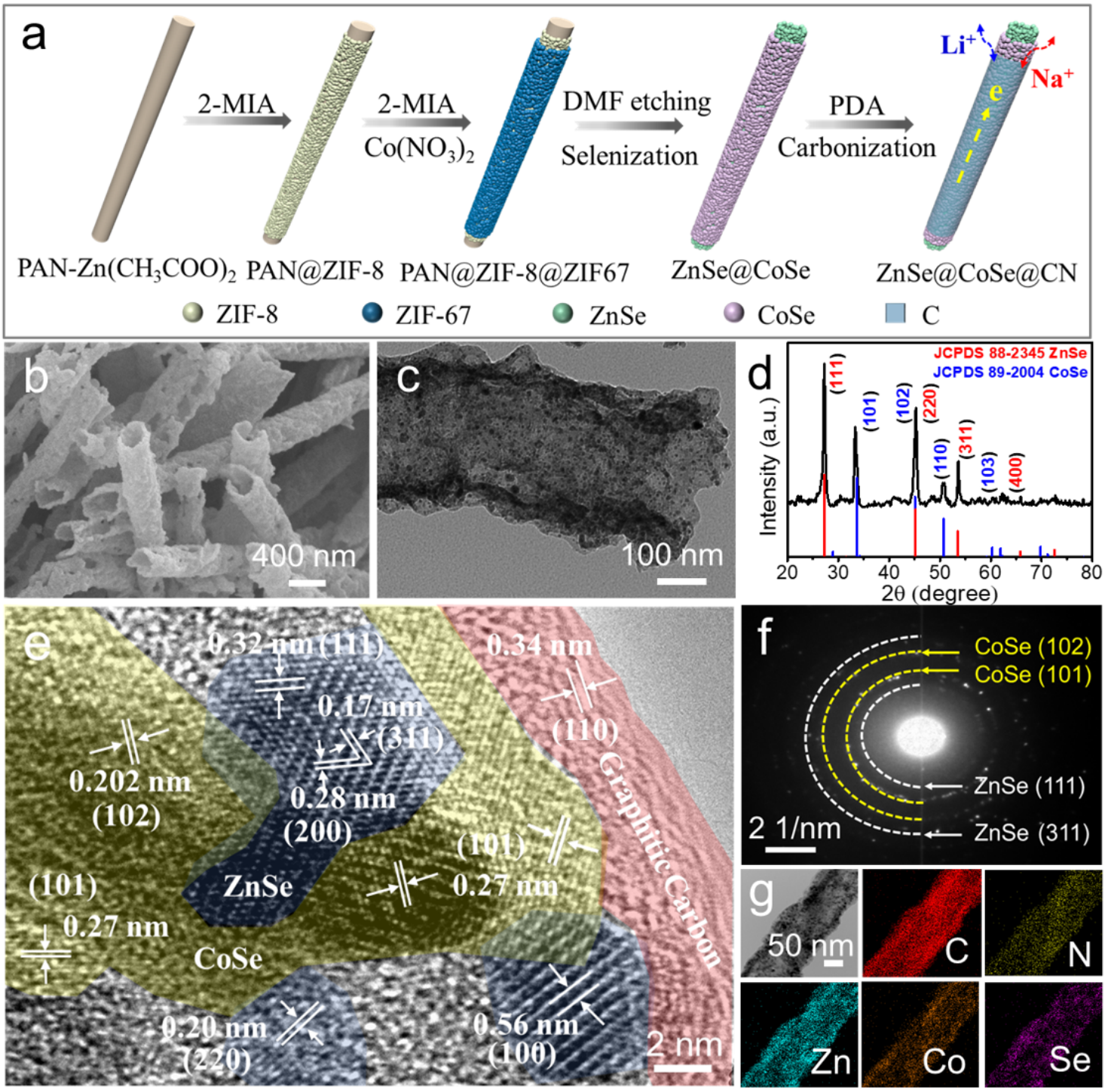

Figure 1

(a) Schematic illustration for the synthetic process of the ZnSe@CoSe@CN composite NTs. (b) SEM, (c) TEM, (d) XRD patterns, (e) HRTEM image, (f) SAED pattern, and (g) elemental mapping images of ZnSe@CoSe@CN.

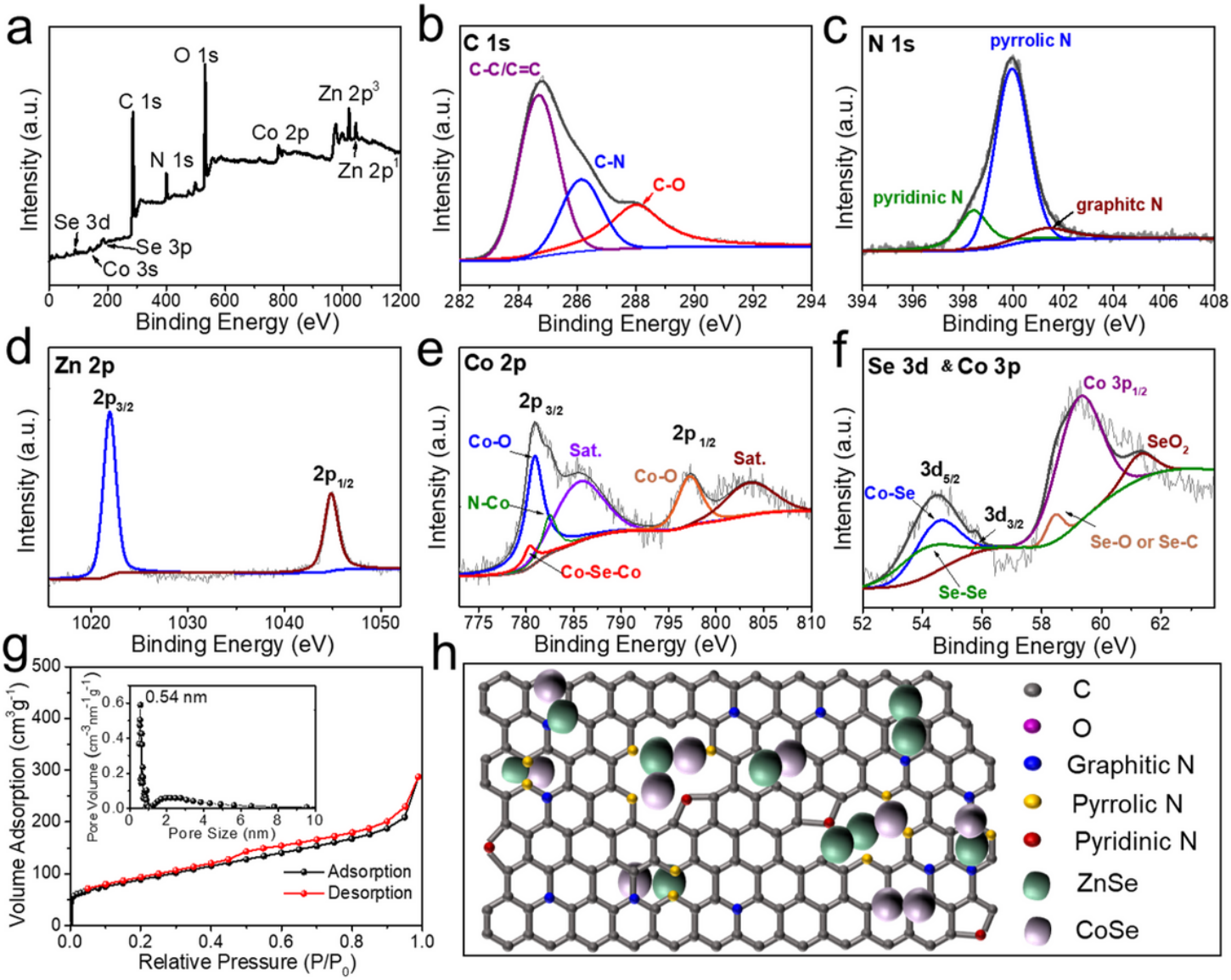

Figure 2

XPS survey spectrum of ZnSe@CoSe@CN (a) and corresponding high-resolution XPS spectra of (b) C 1s, (c) N 1s, (d) Zn 2p, (e) Co 2p, (f) Se 3d and Co 3p. (g) N_2 sorption isotherm of ZnSe@CoSe@CN and inset is corresponding pore size distribution. (h) Schematic representation of N configuration in a carbon matrix.

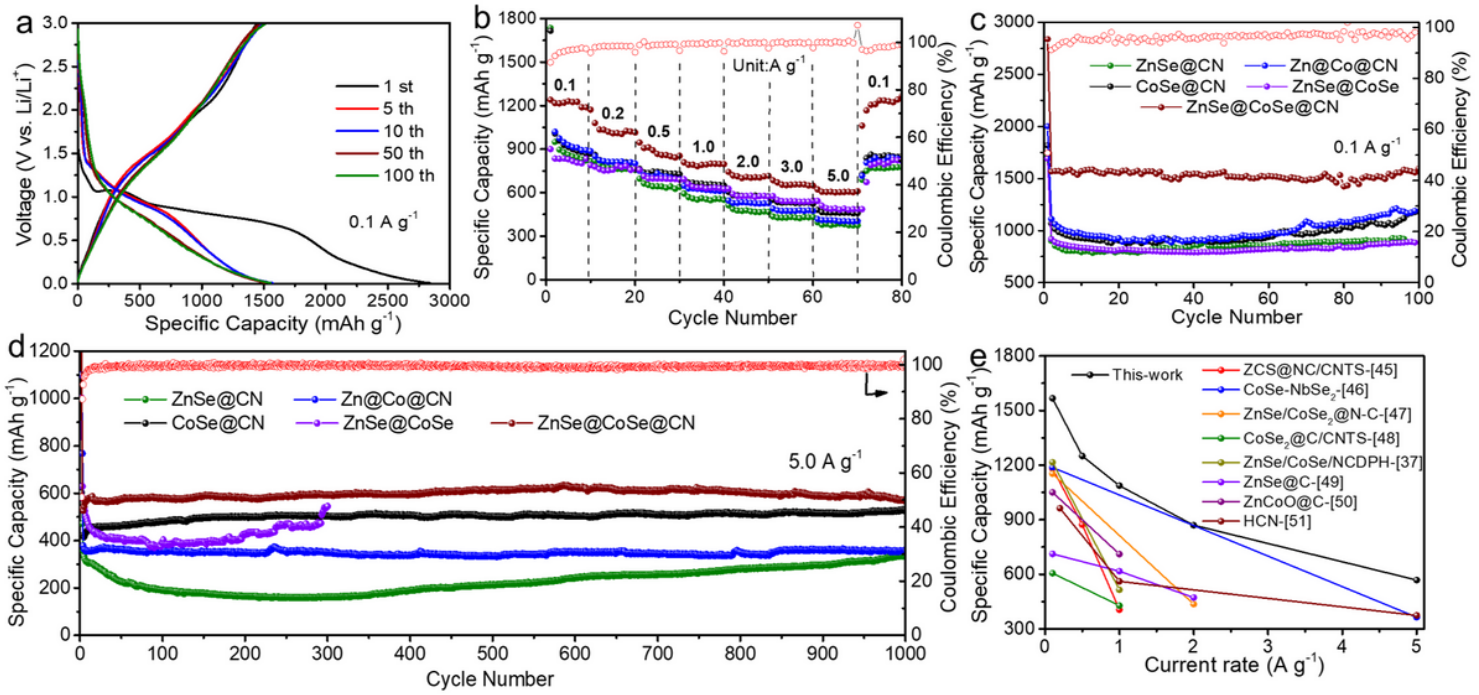

Figure 3

Electrochemical performances of the anodes for LIB. (b) Charge-discharge curves of ZnSe@CoSe@CN at 0.1 A g^{-1}. (c) Rate performance of the as-prepared anodes. Cycling performance of the anodes at (c) 0.1 A g^{-1} for 100 cycles and (d) 5.0 A g^{-1} for 1000 cycles. (e) Comparison of cyclic capability between ZnSe@CoSe@CN and other selenide-based LIB anodes.

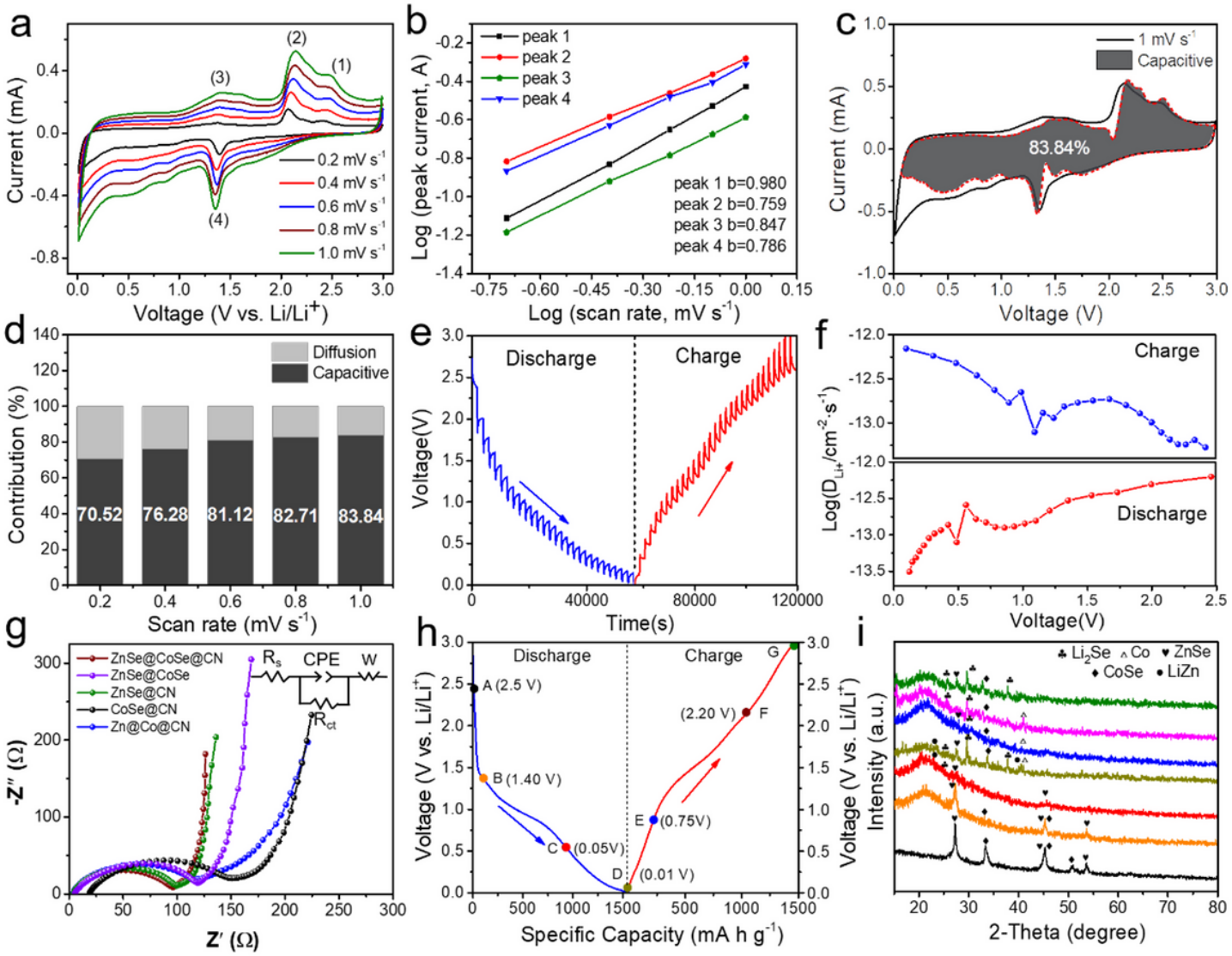

Figure 4

Kinetic analysis of the electrochemical behavior of the ZnSe@CoSe@CN anode for LIBs. (a) CV curves of ZnSe@CoSe@CN at various sweep rates, (b) corresponding b values of the log(scan rate) vs log(peak current) at different oxidation and reduction peaks. (c) Ratio of the capacitive-controlled charge contribution (shaded area) to the total current at a scan rate of 1.0 mV s^{-1}, (d) capacitive contribution ratio at different scan rates, (e) GITT curves, and (f) Calculated lithium-ion diffusion coefficients. (g) Nyquist plots of the anodes, the inset is equivalent circuit model. (h) Charge–discharge curve for the 10 th cycle of ZnSe@CoSe@CN at 0.1 A g^{-1} and (i) the corresponding ex-situ XRD patterns.

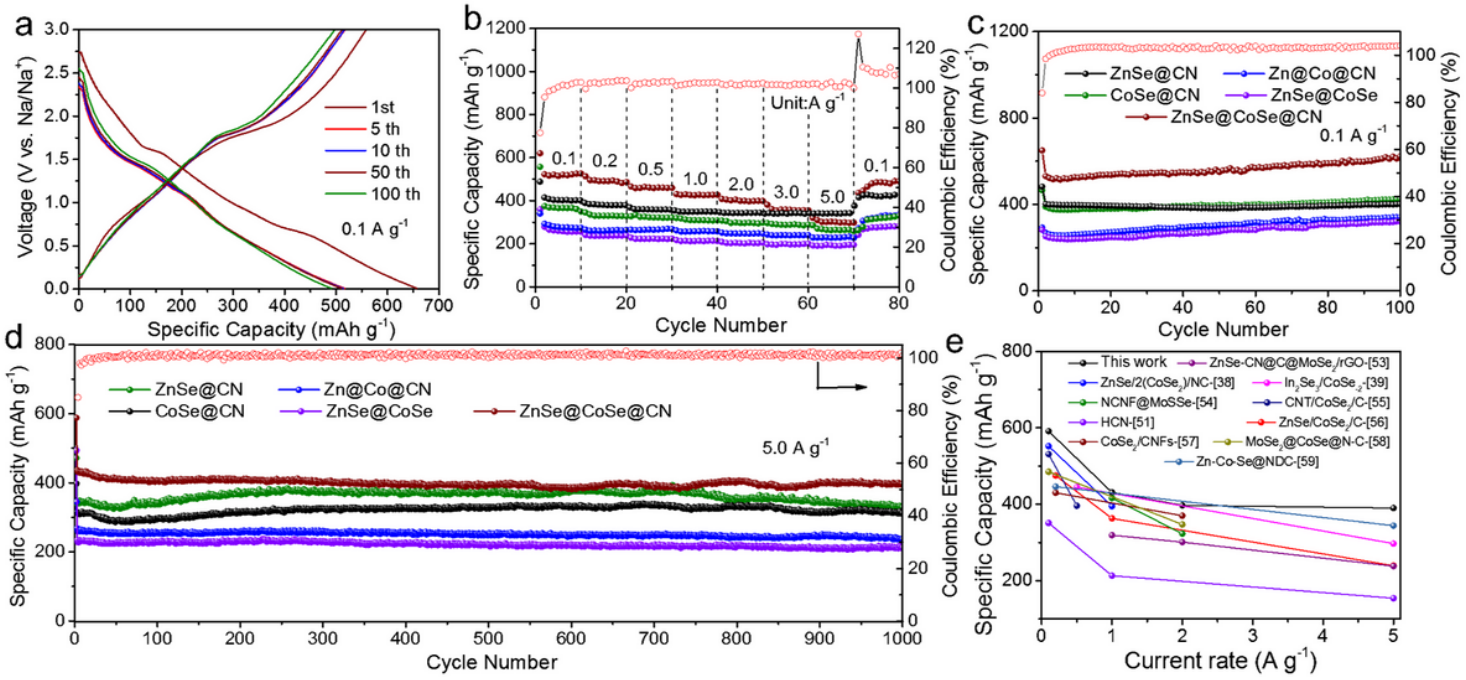

Figure 5

Electrochemical performances of the anodes for SIB. (a) Charge-discharge curves of ZnSe@CoSe@CN at 0.1 A g^{-1}. (b) Rate performance of as-prepared anodes. Cycling performance of the anodes at (c) 0.1 A g^{-1} for 100 cycles and (d) 5.0 A g^{-1} for 1000 cycles. (e) Comparison of cyclic capability between ZnSe@CoSe@CN and other selenide-based SIB anodes.

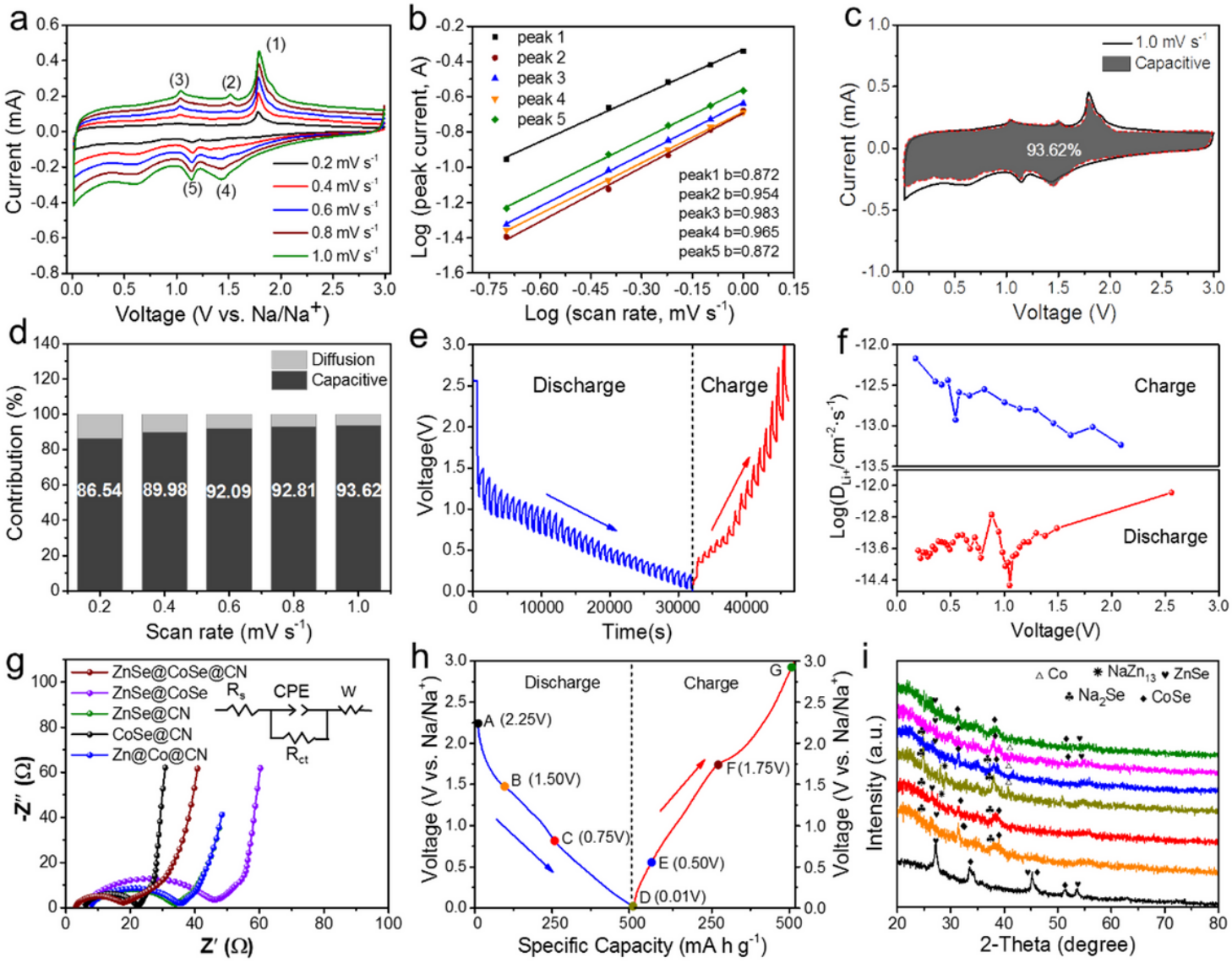

Figure 6

Kinetic analysis of the electrochemical behavior of the ZnSe@CoSe@CN anode for SIBs. (a) CV curves of ZnSe@CoSe@CN at various sweep rates, (b) corresponding b values of the log(scan rate) vs log(peak current) at different oxidation and reduction peaks. (c) Ratio of the capacitive-controlled charge contribution (shaded area) to the total current at a scan rate of 1.0 mV s^{-1}, (d) capacitive contribution ratio at different scan rates, (e) GITT curves, and (f) Calculated lithium-ion diffusion coefficients. (g) Nyquist plots of the anodes, and the inset is the equivalent circuit model. (h) Charge–discharge curve for the 10 th cycle of ZnSe@CoSe@CN at 0.1 A g^{-1} and (i) the corresponding ex-situ XRD patterns.

Supplementary Files

This is a list of supplementary files associated with this preprint. Click to download.

- TOC.png

- SI.docx